Journal of Magnetic Resonance **146,** 20–32 (2000)
doi:10.1006/jmre.2000.2123, available online at http://www.idealibrary.com on IDEAL®

# Phase Angle Measurement from Peak Areas (PAMPAS)

Željko Džakula

*Molecular Simulations, Inc., 9685 Scranton Road, San Diego, California 92121*

E-mail: zdz@msi.com

Received July 30, 1999; revised May 9, 2000

**A new method is described for accurate *P*hase *A*ngle *M*easurement from *P*eak *A*rea*S* (PAMPAS) with the goal of facilitating automated phase correction of NMR spectra. PAMPAS measures phases of isolated NMR peaks by using Fourier analysis of a series of peak areas measured with systematically incremented phase shifts. The calculated phases of individual peaks can be employed to extract the zero- and first-order phase corrections by means of linear regression. The method is accurate, independent of the lineshape, robust, fast, and easy to implement.** © 2000 Academic Press

*Key Words:* **NMR; PAMPAS; phase correction; peak integration; lineshape.**

## 1. INTRODUCTION

Phase-sensitive NMR spectra obtained with Fourier transformation of free-induction decays usually contain peaks of mixed absorptive and dispersive character. A linear combination of real and imaginary parts of the spectrum is used to remedy the spectral phase anomalies (*1*). Traditionally, the trigonometric coefficients of the linear combination are determined empirically. The manual adjustment of the phase corrections, although efficient in the case of 1D and 2D spectra, becomes less convenient in multidimensional NMR spectra. A number of automated phase correction procedures have been proposed (*2–12*) with the goal to replace the conventional, manual approach. The common feature shared among most of the automated methods is that they first determine phases of selected peaks and then subject them to linear regression, which yields zero- and first-order phase corrections to be employed across the entire spectral width (*3, 8*).

In most existing automated methods, the first step, calculation of phases for individual peaks, suffers from a number of weaknesses. The difficulties include the dependence on the lineshape (*3, 6, 7*), sensitivity to the signal-to-noise ratio (*8*), dependence on the precision in measured peak positions (*8*), implicit reliance on high digitization rates (*8, 12*), sensitivity to asymmetric peak shapes that arise due to poor shimming (*2, 8, 12*), sensitivity to baseline imperfections (*3*), and intolerance to peak overlaps (*3*).

The *P*hase *A*ngle *M*easurement from *P*eak *A*rea*S* (PAMPAS) is a novel method that focuses on automated phase measurements for individual, isolated peaks. PAMPAS overcomes the difficulties encountered in this least reliable step in the procedure by imposing a series of phase shifts on the selected peaks and by analyzing the dependence of the resulting peak areas on the imposed phase increments. In addition to the advantages of being accurate, fast, independent of the lineshape, and easy to implement, PAMPAS is robust with respect to experimental noise, baseline imperfections, peak overlaps, peak symmetry, the size of the integration domain, and poor digitization of NMR signals.

## 2. COMPUTATIONAL ASPECTS

### 2.1. Theory

The area under an NMR spectrum is proportional to the size of the first point in the FID. Since this number varies as a cosine function of the phase, the area also is a cosine function of the phase. This rule does not change with the envelope of the FID, and therefore the cosine dependence of the sum of all peak areas on the phase remains valid for any peak shape. The rule is strictly valid for the complete spectrum and is only an approximation for one peak in a complicated spectrum. The following derivations describe a single peak in a complex spectrum and depend on the assumption that the dispersive contributions cancel out for each individual peak. An NMR signal S corresponding to a single peak with an arbitrary phase $\Phi$ is made up of both the absorptive and the dispersive components, A and D:

$$\mathsf{S}(\omega) = \mathsf{A}(\omega)\cos(\Phi) + \mathsf{D}(\omega)\sin(\Phi). \qquad [1]$$

The total area under the peak is

$$\begin{aligned} A_{\text{total}}(\Phi) &= \int_{-\infty}^{\infty} \mathsf{S}(\omega)\,d\omega \\ &= \cos(\Phi) \int_{-\infty}^{\infty} \mathsf{A}(\omega)\,d\omega \\ &= \mathsf{N}\cos(\Phi). \end{aligned} \qquad [2]$$



1090-7807/00 $35.00

The only contribution to the integral originates from the absorptive component of the signal because the dispersive part is antisymmetric. The constant N represents the area under the absorptive curve and includes experimental factors such as the sample concentration and the filling factor. If a phase shift $\Psi$ is imposed on the signal, the total peak area changes as

$$\begin{aligned} A_{\text{total}}(\Phi, \Psi) &= \mathsf{N}\cos(\Phi + \Psi) \\ &= \mathsf{N}\cos(\Phi)\cos(\Psi) - \mathsf{N}\sin(\Phi)\sin(\Psi) \\ &= a\cos(\Psi) + b\sin(\Psi), \end{aligned} \quad [3]$$

where

$$a = \mathsf{N}\cos(\Phi) \quad [4]$$

and

$$b = -\mathsf{N}\sin(\Phi). \quad [5]$$

The unknown initial phase $\Phi$ can be extracted from a series of experimentally determined peak areas $A_i$ obtained at different phase shifts $\Psi_i$. The measured area $A_i$, corresponding to the phase shift $\Psi_i$, is

$$A_i = a\cos(\Psi_i) + b\sin(\Psi_i), \quad i = 1, \ldots, N. \quad [6]$$

A series of measurements establishes a set of linear equations for the Fourier coefficients $a$ and $b$.

$$\begin{bmatrix} \cos(\Psi_1) & \sin(\Psi_1) \\ \cos(\Psi_2) & \sin(\Psi_2) \\ \cos(\Psi_3) & \sin(\Psi_3) \\ \vdots & \vdots \\ \cos(\Psi_N) & \sin(\Psi_N) \end{bmatrix} \begin{bmatrix} a \\ b \end{bmatrix} = \begin{bmatrix} A_1 \\ A_2 \\ A_3 \\ \vdots \\ A_N \end{bmatrix} \quad [7]$$

The unknown phase $\Phi$ follows straightforwardly from the calculated Fourier coefficients $a$ and $b$:

$$\Phi = \text{arctg}(-b/a) + \begin{cases} 0, & a \geq 0 \\ \pi, & a < 0 \end{cases}. \quad [8]$$

The peak intensity also can be found from $a$ and $b$:

$$\mathsf{N} = a/\cos(\Phi). \quad [9]$$

The phase shifts need not be equidistant. At least two measurements have to be done to solve for the two unknowns ($a$ and $b$). The following special cases will be considered:

(1) Two measurements are made ($A_1$ and $A_2$): $A_1$ corresponds to zero phase shift ($\Psi_1 = 0$), and $A_2$ corresponds to $\Psi_2 = \pi/2$. This special case is particularly simple because the matrix from Eq. [7] becomes the $2 \times 2$ unit matrix. Equation [8] for the unknown initial phase becomes

$$\Phi = \text{arctg}(-A_2/A_1) + \begin{cases} 0, & A_1 \geq 0 \\ \pi, & A_1 < 0 \end{cases}. \quad [10]$$

(2) As in case 1, two areas are measured. $A_1$ corresponds to zero phase shift ($\Psi_1 = 0$). $A_2$ corresponds to $\Psi_2 = 2\pi/3$. The phase is calculated from the measured areas as follows:

$$\Phi = \text{arctg}\left[-\frac{2A_2 + A_1}{\sqrt{3}A_1}\right] + \begin{cases} 0, & A_1 \geq 0 \\ \pi, & A_1 < 0 \end{cases} \quad [11]$$

(3) Three measurements are made ($A_1$, $A_2$, and $A_3$) with phase increments of $2\pi/3$ ($\Psi_1 = 0$, $\Psi_2 = 2\pi/3$, $\Psi_3 = 4\pi/3$). The left generalized matrix inverse is used to solve Eq. [7],

$$\begin{aligned} \begin{bmatrix} a \\ b \end{bmatrix} &= \begin{bmatrix} 1 & 0 \\ \cos(2\pi/3) & \sin(2\pi/3) \\ \cos(4\pi/3) & \sin(4\pi/3) \end{bmatrix}^{-1} \begin{bmatrix} A_1 \\ A_2 \\ A_3 \end{bmatrix} \\ &= \frac{1}{3}\begin{bmatrix} 2 & -1 & -1 \\ 0 & \sqrt{3} & -\sqrt{3} \end{bmatrix} \begin{bmatrix} A_1 \\ A_2 \\ A_3 \end{bmatrix}. \end{aligned} \quad [12]$$

Equation [8] for the unknown phase $\Phi$ becomes

$$\Phi = \text{arctg}\left[\frac{\sqrt{3}(A_3 - A_2)}{2A_1 - A_2 - A_3}\right] + \begin{cases} 0, & 2A_1 \geq A_2 + A_3 \\ \pi, & 2A_1 < A_2 + A_3 \end{cases}. \quad [13]$$

(4) The $N$ measurements are made with equidistant phase shifts ranging from $\Psi_1 = 0$ to $\Psi_N = 2\pi(N-1)/N$ with the step $\Delta\Psi = 2\pi/N$. The Fourier coefficients can be found from the overdetermined set of linear equations (Eq. [7]), using generalized matrix inversion or traditional Fourier analysis.

$$\begin{aligned} a &= \frac{1}{\pi}\int_0^{2\pi} A_{\text{total}}(\Phi, \Psi)\cos(\Psi)d\Psi \\ &\approx \frac{1}{\pi}\sum_{i=1}^{N} A_i \int_{\Psi_i - \pi/N}^{\Psi_i + \pi/N} \cos(\Psi)d\Psi \\ &= \frac{1}{\pi}\sum_{i=1}^{N} A_i[\sin(\Psi_i + \pi/N) - \sin(\Psi_i + \pi/N)] \end{aligned} \quad [14]$$

$$b = \frac{1}{\pi}\int_0^{2\pi} A_{\text{total}}(\Phi, \Psi)\sin(\Psi)d\Psi$$

$$\approx \frac{1}{\pi}\sum_{i=1}^{N} A_i \int_{\Psi_i-\pi/N}^{\Psi_i+\pi/N} \sin(\Psi)d\Psi$$

$$= \frac{1}{\pi}\sum_{i=1}^{N} A_i[-\cos(\Psi_i + \pi/N) + \cos(\Psi_i + \pi/N)] \quad [15]$$

The unknown phase $\Phi$ follows straightforwardly from the Fourier coefficients $a$ and $b$ (Eq. [8]).

### *2.2. Algorithm*

In practice, cases 1–4 yield identical results and only differ in the level of complexity. The recommended PAMPAS procedure relies therefore on the simplest protocol (case 1) and consists of the following eight steps:

(1) Calculate the magnitude mode spectrum.
(2) Identify an isolated peak.
(3) Select integration limits. The domain of integration should be centered at the peak and significantly wider than the peak width.
(4) Calculate the phase-sensitive mode spectrum. Use the phase-sensitive mode for further manipulations.
(5) Calculate the average value of a few tail points at both ends of the integration domain. This average value will be used to estimate the baseline. A horizontal or tilted straight baseline yields satisfactory results.
(6) Sum up all the values of the spectrum within the integration domain. The result is stored as $A_1$ (peak area with no phase shift). Apply the correction for baseline offset using results from step 5.
(7) Change the phase of the spectrum by $\pi/2$ (case 1). Repeat steps 5 and 6 to measure $A_2$.
(8) Use Eq. [10] to find the unknown initial phase.

In the special case when $A_1 \ll A_2$ ($\Phi \approx \pm\pi/2$), the denominators in all the equations for $\Phi$ (Eqs. [10, 11] and [13, 14]) contain combinations of measured areas that are likely to vanish. To avoid division by zero, the phase of the peak should be shifted by an angle different from $n\pi$ before steps 5–8 are employed. The modified algorithm takes advantage of the fact that the new phase implies $A_1 \neq 0$.

The procedure can be applied repeatedly to a number of suitable peaks. When the phases of several peaks across the spectrum are known, the zero- and first-order corrections can be found by linear regression.

## 3. APPLICATIONS

Figure 1 illustrates an application of the procedure outlined above on the $^1$H–$^{15}$N HSQC spectrum of $^{15}$N enriched monocyte chemoattractant protein-1 (MCP-1) (*13*). The phase along the proton dimension of the already phased spectrum is increased using randomly chosen zero- and first-order phase increments of 167.1° and 233.0°, respectively. The resulting spectrum is subjected to PAMPAS calculations. Figures 1a–1f display a series of cross sections through isolated peaks whose unknown initial phases need to be determined with PAMPAS. Also shown are the same peaks after being phase-corrected using phase angles from Table 1 (last column). The peak areas

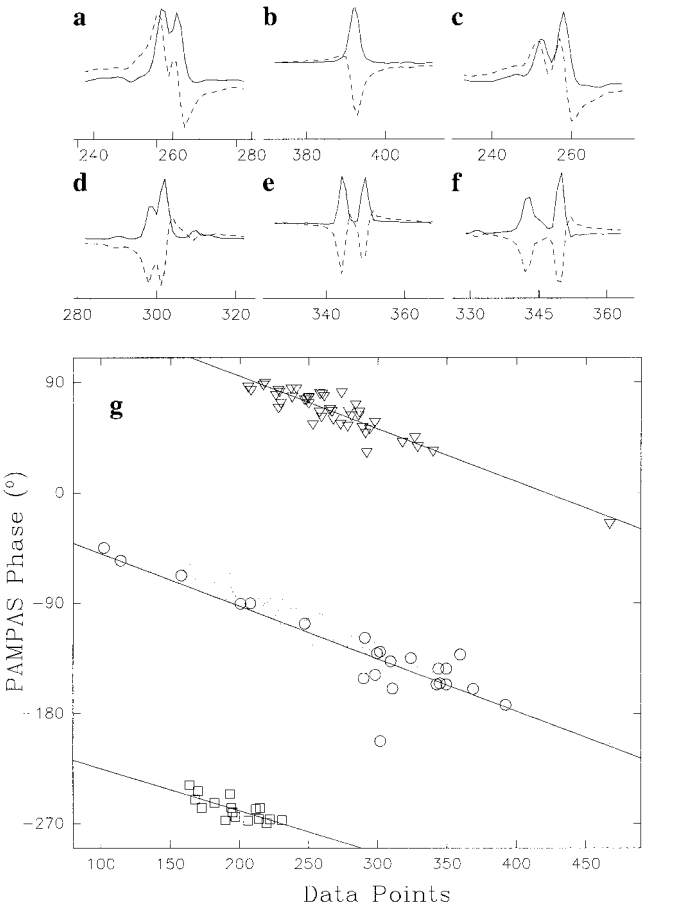


**FIG. 1.** (a–f ) Examples of PAMPAS calculations performed on $^1$H cross sections through a set of isolated peaks from the $^1$H–$^{15}$N HSQC spectrum of $^{15}$N enriched monocyte chemoattractant protein-1 (*14*); (g) linear regression of PAMPAS phases for all peaks in the spectrum. Before applying PAMPAS, zero- and first-order phase errors of 167.1° and 233.0°, respectively, are imposed along the hydrogen dimension of the already phased spectrum. Dashed lines in insets (a–f ) represent peaks before PAMPAS phase correction. Phase-corrected peaks are displayed in solid lines. The peaks correspond to the following residues: 56K, 66H (inset a), 60V (inset b), 35K, 48A (inset c), 61Q (inset d), 23Q, 6N (inset e), and two unassigned peaks (inset f ). Circles in inset (g) denote phases calculated for peaks that are not folded. Triangles and squares refer to peaks that are out of phase by $\pi$ or by $-\pi$, respectively. Dots represent the same results as triangles and squares after being shifted by $\pi$. A linear regression performed on all three groups of phases (solid lines in inset (g)) yields the following results: zero-order phases of 172.9°, 181.0°, and 169.6°, first-order phases of 217.1°, 220.2°, and 176.6°, and regression coefficients of 0.885, 0.924, and 0.757 for circles, triangles, and squares, respectively.

$A_1$ and $A_2$ (Table 1) are combined according to Eq. [10] to yield the phase corrections (Table 1). Most of the peaks are integrated over a 41-point wide domain. For 19 peaks, the size of the domain needs to be reduced to 15 or 35 points to avoid interference from nearby peaks (Table 1). The peaks 23Q and 6N must be treated as a single cluster, with the integration domain centered between them (Table 1, Fig. 1e). The same holds for a pair of unassigned peaks (Table 1, Fig. 1f). In all cases, the application of PAMPAS results in adequately phased peaks with one exception of a weak, unassigned peak at (7.37 ppm, 123.8 ppm). The linear regression of PAMPAS phases for all peaks in the spectrum reproduces the zero- and first-order phase errors within 10° and 15°, respectively (Fig. 1g).

Figures 2–12 show how PAMPAS precision and accuracy depend on noise, integration domain width, peak picking errors, first-order phase errors, solvent signal, baseline slope, peak overlap, peak asymmetry, spectral resolution, line broadening, and lineshape. For each one of these factors, and for each value of each factor, PAMPAS phase corrections are employed on a set of spectra obtained from the same starting spectrum by incrementing its zero-order phase over the range $(0, 2\pi)$ in steps of $\pi/4$. For each value of the phase error, $N_{\text{noise}}$ random noise sequences are added to the spectrum. The noise is generated using a uniform distribution within a preselected noise interval. The noise level is expressed for each peak separately in dB. Differences between the actual phase errors and the values calculated with PAMPAS are averaged over the whole set of $N_{\text{noise}}$ spectra corresponding to each fixed value $n\pi/4$ ($n = 0, \ldots, 7$) of the phase error. Averaging over $N_{\text{noise}}$ different noise sequences is performed separately for each phase error value to isolate the stochastic effects of the randomly generated noise sequences from the deterministic effects of the systematically varied phase angles. The data points and error bars in Figs. 2a–12a depict the averaged values and the standard deviations, which stand for the accuracy and precision of PAMPAS, respectively. The continuous lines in Figs. 2a–12a represent maximal differences between true phase errors and PAMPAS results. The maxima are taken over the whole set of phase errors and noise sequences.

A simulated 1D $^1$H NMR spectrum of alanine is the starting point for calculations. The widths and the scalar coupling splittings of peaks corresponding to the beta protons (1.5 ppm), the alpha proton (4.1 ppm), and the amide (8.2 ppm) are exaggerated to facilitate visual inspection of the results. The same noise level (−5.2 dB relative to the $\alpha$ peak height), straight and horizontal baseline, fixed peak widths, zero solvent signal, no first-order phase error, absent peak asymmetry and overlap, uniform resolution (512 points in the data set), and Lorentzian lineshapes are used in all calculations unless stated otherwise. Twenty noise sequences are generated for each phase error value in all figures except in Fig. 2 ($N_{\text{noise}} = 100$) and Fig. 9 ($N_{\text{noise}} = 5$). The parameters for PAMPAS integration also are kept unchanged unless stated differently: the width of the integration domain is four times larger than the amide peak width, its center matches the peak position, and the baseline is corrected using a straight, horizontal line.

Figure 2a shows the effects of the signal-to-noise ratio on the accuracy (data points) and precision (error bars) in the calculated peak phases. The noise level varies in these calculations from none to 0 dB (Figs. 2c–2e show peaks with −3 dB noise). PAMPAS phases remain within 5° from the actual phases with minimal dispersion across most of the range of noise levels studied (Fig. 2a). Figure 2b shows the angular profile of the differences between true phase errors and PAMPAS corrections calculated across the whole 360° range in 1° steps. The line on the top represents the maximum deviation, the second line from the bottom depicts the average, and the remaining two lines show average ± standard deviation. Only the worst case ($\beta$ peak) is shown.

The effect of the size of the integration domain is displayed in Fig. 3a. The variable domain width ranges from a bare minimum (the peak itself, no baseline, Figs. 3b, 3d, and 3f) to four times the amide peak width (Figs. 3c, 3e, and 3g). Narrow integration domains invariably lead to PAMPAS errors in excess of 20° (Fig. 3a). PAMPAS errors of ≈5° can be expected when the domain width exceeds 200% of the peak width (Fig. 3a).

The significance of the errors in the measured peak positions is studied in Fig. 4a. The integration domain center deviates from the actual peak position by up to ≈100% of the peak width (Figs. 4b–4g). PAMPAS errors of less than 10° require that the distance from the true peak position to the center of the integration domain does not surpass 25% of the peak width (Fig. 4a).

Figure 5 shows that PAMPAS errors remain small (<5°) over a large range of first-order phase error values imposed on the spectrum. Peaks that are located far from the phasing pivot can display weak oscillatory behavior (Figs. 5f–5i), but the noise masks the oscillations to a large extent (Figs. 5d–5e). The oscillation amplitudes increase with the distance from the phasing pivot. The oscillatory patterns strongly depend on the peak position relative to the sampling points (Figs. 5f–5i). Neither the amplitudes nor the oscillatory patterns vary with the integration domain width, as evidenced by the two curves in Fig. 5f. The curve in Fig. 5g appears to be V-shaped because it represents absolute values of PAMPAS errors. Zero-order phase errors $n\pi/4$ ($n = 0, \ldots, 7$) do not influence PAMPAS errors at all, as illustrated by data points in Figs. 5f–5i.

Intensity of a dispersive, wide solvent signal (water at 4.75 ppm) significantly influences PAMPAS results when the ratio between the water signal and the $\beta$ peak varies from 0:1 to $10^4$:1 (errors > 10°; Fig. 6a). The results for the $\alpha$ peak are not shown because it is completely masked by the solvent signal (Fig. 6b).

The baseline tilt exhibits minimal influence on PAMPAS results, as shown by Fig. 7a. The examined slope values, expressed in intensity units per data point, run from −50 (Figs.

**TABLE 1**
**Measured Peak Areas and Calculated Phase Errors along the $^{1}$H Dimension for All Peaks in $^{1}$H–$^{15}$N HSQC Spectrum of $^{15}$N Enriched Monocyte Chemoattractant Protein-1 (*13*)**

| Residue assignment | $^{1}$H (ppm) | $^{15}$N (ppm) | $A_1^{a,b}$ | $A_2^{b,c}$ | Phase$^{d}$ Φ (°) |
|---|---|---|---|---|---|
| 3D | 8.43 | 118.0 | 640.23 | 2138.47 | 73.3 |
| 4A | 8.20 | 122.6 | 531.20 | 2161.41 | 76.1 |
| 5I[f] | 7.97 | 117.3 | 651.18 | 1617.16 | 68.1 |
| 6N | 8.17 | 116.6 | 766.08 | 3419.27 | 77.3 |
| 6N[g] | 6.93 | 123.5 | −6403.65 | −4740.75 | −143.4 |
| 6N[f] | 7.38 | 123.5 | −2895.01 | −2649.88 | −137.5 |
| 7A | 7.54 | 122.4 | 912.50 | 1454.30 | 57.8 |
| 9V | 8.89 | 118.6 | −162.32 | 994.02 | −260.7 |
| 10T | 8.72 | 113.0 | −5.89 | −862.17 | −90.3 |
| 11C | 8.67 | 119.4 | −255.13 | 1235.99 | −258.3 |
| 12C | 7.72 | 115.0 | 282.72 | 884.77 | 72.2 |
| 13Y[f] | 9.22 | 120.8 | −273.15 | 550.76 | −243.6 |
| 14N | 6.99 | 112.2 | 1780.03 | 1208.31 | 34.1 |
| 14N | 7.69 | 112.2 | 1027.01 | 2049.83 | 63.3 |
| 14N | 7.65 | 116.4 | 594.56 | 807.28 | 53.6 |
| 15F | 8.32 | 114.9 | 209.29 | 1014.97 | 78.3 |
| 16T[f] | 8.60 | 114.3 | 28.42 | 884.84 | 88.2 |
| 17N | 6.92 | 124.0 | −3398.60 | −1554.76 | −155.4 |
| 17N | 7.63 | 124.0 | −1597.94 | −2979.86 | −118.2 |
| 17N | 8.74 | 124.2 | 31.64 | 522.24 | 86.5 |
| 18R | 7.93 | 119.5 | 832.51 | 1449.17 | 60.1 |
| 19K | 7.63 | 119.7 | 1631.58 | 1877.12 | 49.0 |
| 20I | 5.32 | 122.8 | 1607.43 | −752.30 | −25.0 |
| 21S | 8.28 | 119.5 | 244.51 | 3002.79 | 85.3 |
| 22V | 8.44 | 123.4 | 227.45 | 1798.25 | 82.7 |
| 23Q[f] | 8.17 | 117.2 | 351.88 | 1661.63 | 78.0 |
| 23Q[e,f] | 7.53 | 123.4 | −3649.89 | −2240.09 | −148.4 |
| 23Q[g] | 6.86 | 123.4 | −6403.65 | −4740.75 | −143.4 |
| 24R | 7.86 | 113.9 | 1013.89 | 1511.60 | 56.1 |
| 25L | 7.61 | 118.5 | 1232.14 | 803.05 | 33.0 |
| 26A | 9.30 | 121.4 | −599.27 | 980.83 | −238.5 |
| 27S[f] | 8.20 | 119.8 | −543.49 | −1792.86 | −106.8 |
| 28Y | 8.64 | 114.6 | −87.63 | 1313.52 | −266.1 |
| 29R | 8.63 | 116.0 | −312.32 | 1380.71 | −257.2 |
| 30R[f] | 9.06 | 121.0 | −470.45 | 1539.88 | −253.0 |
| 31I | 8.72 | 122.3 | 150.47 | 1424.71 | 83.9 |
| 32T[f] | 8.45 | 114.3 | 244.54 | 649.14 | 69.3 |
| 33S[f] | 7.80 | 114.6 | 529.45 | 742.48 | 54.5 |
| 35K | 8.13 | 117.6 | 1373.01 | 2039.80 | 56.0 |
| 36C | 7.16 | 113.4 | 1064.36 | 1086.64 | 45.5 |
| 38K[e,f] | 6.72 | 123.2 | −1059.13 | −1183.71 | −131.8 |
| 39E | 8.58 | 122.1 | 4.42 | 1990.67 | 89.8 |
| 40A[f] | 8.42 | 119.7 | −67.71 | 1325.68 | −267.1 |
| 41V | 8.56 | 119.1 | −11.26 | 1294.70 | −269.5 |
| 42I | 8.91 | 122.0 | −474.20 | 1062.27 | −245.9 |
| 43F | 9.37 | 112.4 | 417.67 | −1017.59 | −67.6 |
| 44K | 8.95 | 121.5 | −56.96 | 1241.29 | −267.3 |
| 45T | 9.24 | 115.1 | −453.41 | 1270.09 | −250.3 |
| 46I | 8.48 | 113.6 | 187.81 | 1057.35 | 79.9 |
| 47V[e,f] | 7.19 | 123.7 | −864.93 | −865.24 | −134.9 |
| 48A | 8.06 | 117.6 | 354.92 | 2248.67 | 81.0 |
| 49K | 7.13 | 116.5 | 1337.09 | 1039.17 | 37.8 |
| 50E | 8.53 | 120.3 | −69.16 | 1100.88 | −266.4 |
| 51I | 9.18 | 119.2 | −256.36 | 1117.27 | −257.0 |
| 52C | 8.86 | 123.6 | −98.62 | 999.20 | −264.3 |
| 53A | 9.95 | 112.2 | 523.11 | −763.14 | −55.5 |
| 56K | 8.06 | 115.5 | 1217.39 | 2764.73 | 66.2 |

**TABLE 1**—*Continued*

| Residue assignment | $^{1}$H (ppm) | $^{15}$N (ppm) | $A_1^{a,b}$ | $A_2^{b,c}$ | Phase$^{d}$ $\Phi$ (°) |
|---|---|---|---|---|---|
| 57Q | 7.59 | 116.6 | 1160.88 | 1505.15 | 52.3 |
| 58K | 8.81 | 112.5 | −9.04 | −915.49 | −90.5 |
| 59W | 8.74 | 114.1 | −65.90 | 1534.65 | −267.5 |
| 59W | 10.11 | 115.7 | 1329.99 | −1329.59 | −44.9 |
| 60V$^{e}$ | 6.30 | 112.0 | −1208.32 | 946.51 | −173.0 |
| 61Q | 7.48 | 123.3 | −3054.14 | −3685.12 | −129.6 |
| 61Q | 7.27 | 119.2 | 1158.42 | 1019.93 | 41.3 |
| 61Q$^{f}$ | 6.60 | 123.3 | −2814.08 | −1020.60 | −160.0 |
| 62D | 8.90 | 118.0 | −391.70 | 1721.32 | −257.1 |
| 63S$^{f}$ | 8.04 | 116.8 | 568.53 | 1081.07 | 62.2 |
| 64M | 8.17 | 120.3 | 322.58 | 1061.69 | 73.0 |
| 65D | 7.96 | 116.1 | 659.43 | 1678.58 | 68.5 |
| 66H | 8.02 | 115.5 | 565.36 | 2917.35 | 79.0 |
| 67L | 8.33 | 118.9 | 89.39 | 1103.18 | 85.3 |
| 68D | 8.89 | 119.7 | −244.32 | 1543.35 | −261.0 |
| 69K | 7.68 | 117.0 | 836.46 | 1891.91 | 66.1 |
| 70Q$^{f}$ | 7.76 | 116.9 | 810.80 | 1585.03 | 62.9 |
| 71T | 7.95 | 111.7 | 772.41 | 1786.46 | 66.6 |
| 72Q | 8.19 | 120.6 | 569.99 | 2328.79 | 76.2 |
| 75K | 8.46 | 121.2 | 426.28 | 4078.74 | 84.0 |
| 76T | 7.79 | 119.3 | 1770.33 | 4135.77 | 66.8 |
| Null$^{f}$ | 8.04 | 114.6 | 70.92 | 439.81 | 80.8 |
| Null$^{f}$ | 7.85 | 119.9 | 79.56 | 551.82 | 81.7 |
| Null | 7.48 | 122.5 | −388.82 | 161.09 | −202.5 |
| Null$^{f}$ | 7.37 | 123.8 | −886.71 | −328.36 | −159.7 |
| Null | 7.51 | 123.8 | −3973.15 | −4583.37 | −130.9 |
| Null | 7.64 | 123.7 | −4456.82 | −2433.89 | −151.3 |
| Null$^{e,h}$ | 6.86 | 123.8 | −5345.76 | −2372.76 | −156.1 |
| Null$^{e,h}$ | 6.95 | 123.7 | −5345.76 | −2372.76 | −156.1 |

[a] The areas $A_1$ correspond to the phase shift $\Psi_1 = 0$.
[b] Integration domain is 41 points wide unless stated otherwise.
[c] The areas $A_2$ correspond to the phase shift $\Psi_2 = \pi/2$.
[d] Equation [10] is used to extract the phase error from the area measurements.
[e] The phase is shifted by $\pi/4$ prior to applying PAMPAS.
[f] Integration domain is 15 points wide.
[g] Integration domain is centered between 6N (6.93 ppm, 123.5 ppm) and 23Q (6.86 ppm, 123.4 ppm).
[h] Integration domain is 35 points wide and centered between the unassigned peaks located at (6.86 ppm, 123.8 ppm) and (6.95 ppm, 123.7 ppm).

7b, 7d, and 7f) to 50 (Figs. 7c, 7e, and 7g) without changing calculated phases.

To inspect the influence of overlapping peaks on PAMPAS phases, a set of new peaks is introduced into the simulated alanine spectrum. It corresponds to an additional alanine molecule with slightly shifted resonances and 60% lower peak intensities. The centers of the integration domains are placed in the middle of each peak pair (Figs. 8b–8g). Figure 8a represents the errors in PAMPAS phases caused by gradual divergence of the resonances from two different alanines.

Figure 9a shows how the peak asymmetry affects PAMPAS results. The effects of poor shimming are modeled using equations from the Appendix. The product $\lambda(\partial^2 B/\partial z^2)\delta^2$, which measures the field inhomogeneity (see Eqs. [A1]–[A3]), increases in these calculations from zero (Figs. 9b, 9d, and 9f) to 5 rad/s (Figs. 9c, 9e, and 9g). When $\lambda(\partial^2 B/\partial z^2)\delta^2 > 2$ rad/s, the errors in PAMPAS phases can be kept below 10° by widening the integration domain (not shown).

Figure 10a illustrates the effects of the spectral resolution on the calculated phase errors. The number of the sampling points decreases from 512 (Figs. 10b, 10d, and 10f) to 64 (Figs. 10c, 10e, and 10g) without increasing the errors in PAMPAS results beyond ≈30°.

The application of a series of exponential window functions with increasing line broadening shows that magnified peak widths do not produce noticeable enlargement of PAMPAS errors (Fig. 11a). The line broadening factor extends from zero (Figs. 11b, 11d, and 11f) to 100 $s^{-1}$ (Figs. 11c, 11e, and 11g). The width of the integration domain is one-third the size of the portion of spectrum shown in insets b–g in Fig. 11.

To study the effects of various lineshapes, PAMPAS calculations are repeated on the same data processed with the

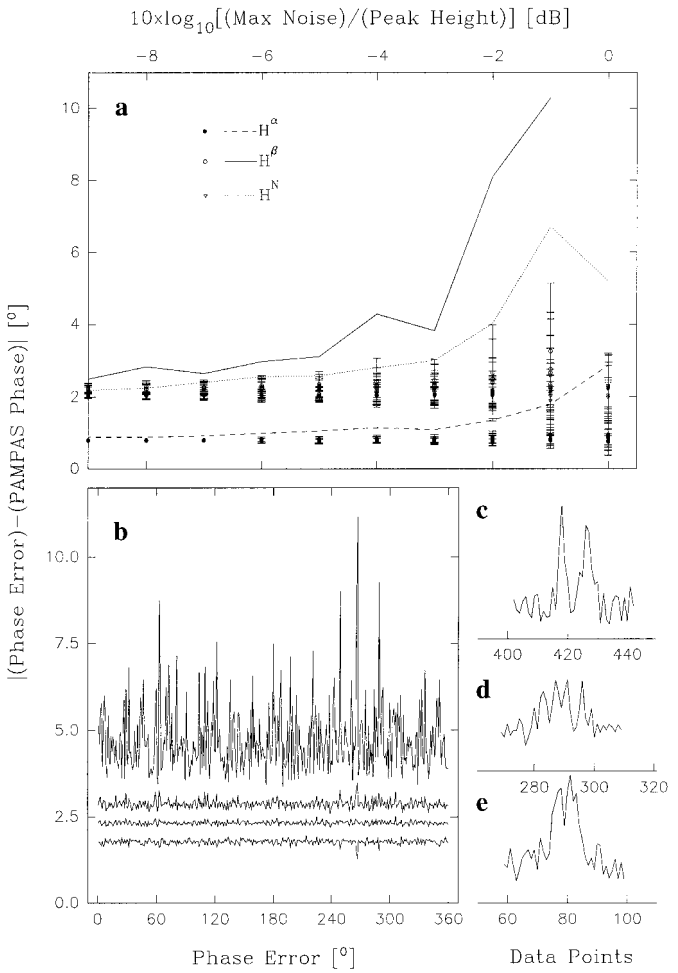


**FIG. 2.** (a) The effect of the signal-to-noise ratio on errors in calculated peak phases; (b) the angular profile of the differences between true phase errors and PAMPAS results; (c–e) examples of $\beta$-, $\alpha$-, and amide peaks with $-3$ dB noise superimposed on the simulated spectrum. A simulated alanine proton spectrum, subjected to a series of zero-order phase shifts, is used to calculate PAMPAS errors. Data points in inset (a) represent PAMPAS errors averaged over 100 randomly generated noise sequences ($-3$ dB relative to the $\beta$-peak) for each of eight fixed phase errors $n\pi/4$ ($n = 0, \ldots, 7$). Data points in inset (a) represent the $\alpha$ proton (filled circles), $\beta$ protons (open circles), and the amide peak (triangles). The dashed, solid, and dotted continuous lines in inset (a) represent maximum PAMPAS errors for $\alpha$-, $\beta$-, and amide peaks, respectively. The maxima are taken over the whole set of phase errors and noise sequences. The top line in inset (b) indicates the angular profile of the maximum PAMPAS error for the $\beta$-peak. The average PAMPAS error is represented by the second line from the bottom. The remaining lines correspond to average $\pm$ standard deviation. The calculations are performed over the whole 360° range in 1° steps. Maximum, average, and standard deviation values are calculated over 100 noise sequences ($-3$ dB relative to the $\beta$-peak), generated separately at each 1° increment. The integration domain is 41 points wide.

following apodization functions: exponential line broadening, Gaussian window, sine bell, squared sine bell, skewed sine bell, skewed squared sine bell, Kaiser window, and trapezoidal function (Figs. 12b–12i, respectively). The type of apodization and the resulting lineshape do not cause any detectable effects on PAMPAS results for any of the window functions studied (Fig. 12a).

All calculations are performed with the FELIX software package for NMR processing and analysis (*14*).

## 4. DISCUSSION

The accuracy of PAMPAS calculations is influenced by a number of factors that are difficult to control once the spectrum has been collected. Adverse effects of unfavorable experimental NMR conditions, such as low sample concentration, instrumental imperfections, inappropriate choice of the pulse program, insufficient solvent suppression, inadequate initial

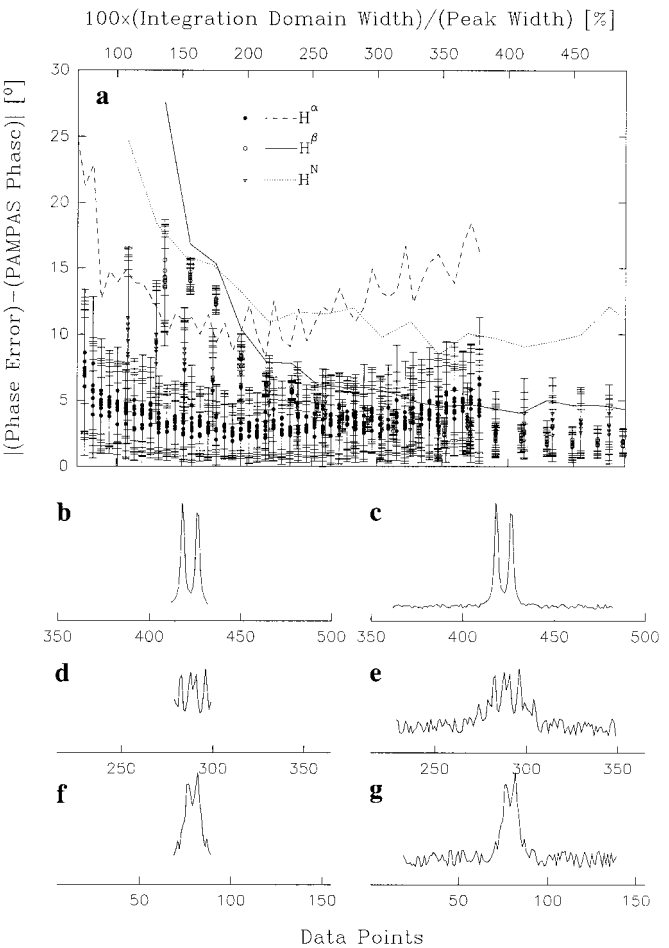


**FIG. 3.** (a) PAMPAS error as a function of the integration domain width; (b–g) examples showing the range of integration domain widths used to calculate data points in inset (a). The same simulated NMR peaks are used as in Figs. 1b–1g. The averages (data points) and standard deviations (error bars) are calculated over a set of 20 noise sequences, generated separately for each fixed phase error value $n\pi/4$ ($n = 0, \ldots, 7$). The maximum PAMPAS errors (continuous lines) are taken over all phase error values and noise sequences. Insets (b), (d), and (f) represent minimal integration domain widths. Insets (c), (e), and (g) show integration domains 10 times wider than the $\beta$-peak. The noise is fixed at $-5.2$ dB relative to the $\alpha$-peak. The meanings of the data point symbols and continuous lines in inset (a) are the same as in Fig. 2a.

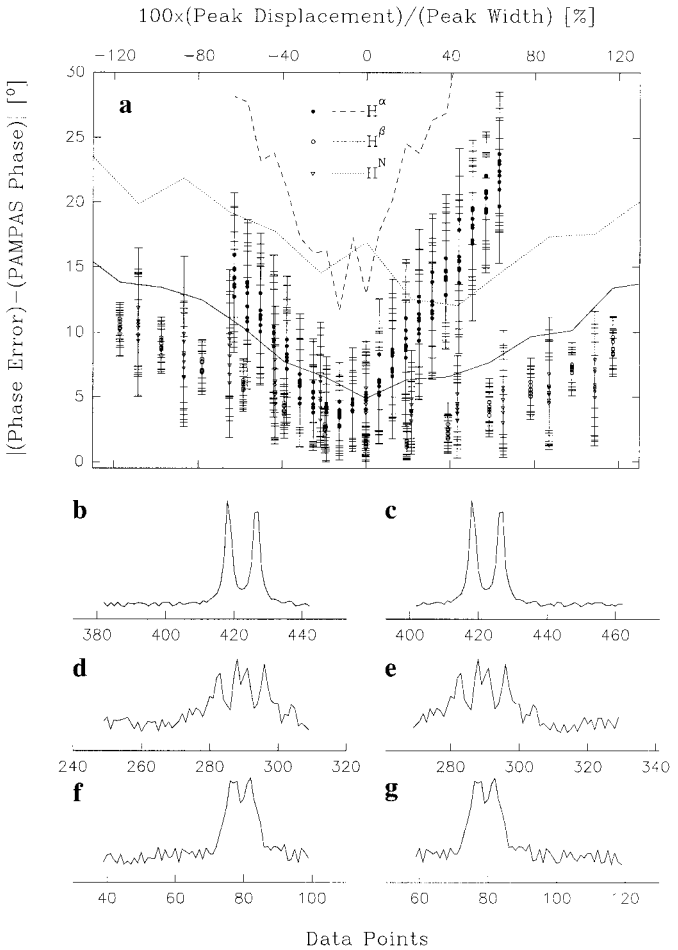


**FIG. 4.** (a) PAMPAS error as a function of the offset between the peak position and the center of the integration domain; (b–g) examples of peaks and misplaced integration domains used to calculate data points in inset (a). The data point symbols and continuous lines have the same meaning as in Fig. 2a. Twenty noise sequences (−5.2 dB relative to $\alpha$-peak) are used. Phase error values are the same as in Figs. 2a–3a. The integration domain width is 121 points.

acquisition delays, small number of acquired data points, and unsatisfactory homogeneity of the magnetic field, cannot be eliminated when the processing reaches the stage of spectral phasing. Spectral characteristics inherent to the sample, such as poor chemical shift dispersion and large natural linewidths, are not helpful either and are even less manageable. It will be shown, however, that a judicious choice of parameters for PAMPAS calculations can reduce the sensitivity of PAMPAS results to those factors. For example, PAMPAS phases can be improved by picking the most suitable PAMPAS algorithm (Eqs. [10]–[15]), adjusting the integration domain width, carefully positioning the center of the integration domain, choosing the most appropriate treatment for the baseline correction, and including multiple peaks into the integration domain. The results of simulations shown in Figs. 2–12 provide guidelines for optimizing PAMPAS parameters.

Fortunately, the signal-to-noise ratio, although often the most noticeable (and irritating) among experimental factors, hardly influences PAMPAS results at all (Fig. 2a). PAMPAS owes its remarkable robustness with respect to noise to the fact that the integration procedure accumulates the signal while averaging random noise to zero. The applicability of PAMPAS to weak peaks (Fig. 2e) contrasts the sensitivity of the line-shape methods to noise (*8*).

Somewhat less conspicuous, yet much more consequential for PAMPAS, are the errors in the measured peak positions. Normally, the integration domain is centered at the middle of

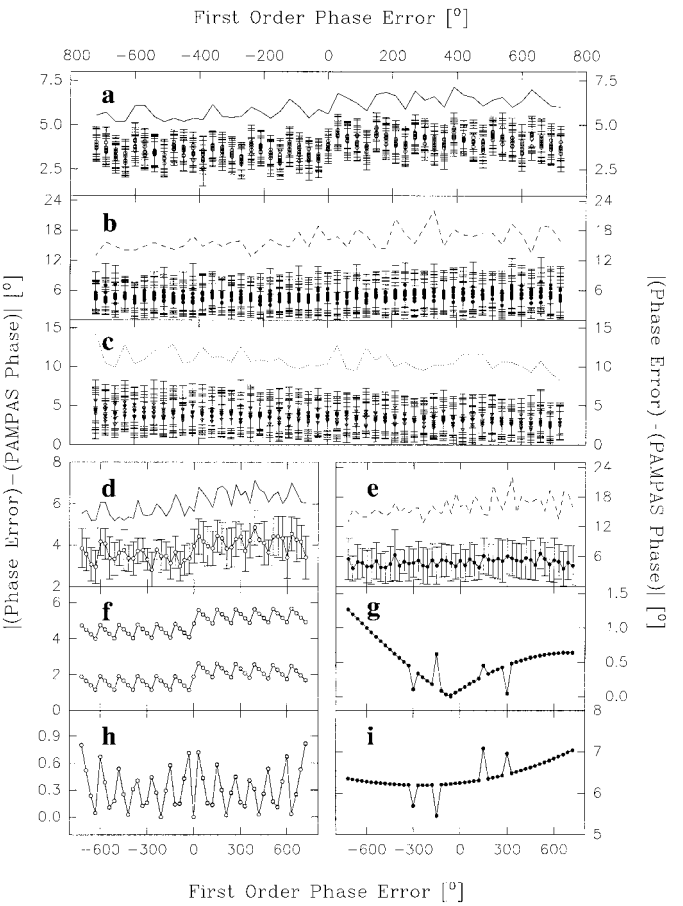


**FIG. 5.** Effects of the first-order phase error on PAMPAS calculations. Insets (a–c) show PAMPAS errors for $\beta$-, $\alpha$-, and amide peaks, respectively. Eight zero-order phase errors $n\pi/4$ ($n = 0, \ldots, 7$) are used for each first-order phase error data point in insets (a–c, f–i). Insets (d, e) show results for peaks $\beta$ and $\alpha$, respectively, with zero-order phase error equal to $\pi/4$. Twenty noise sequences (−5.2 dB relative to the $\alpha$-peak) are generated in insets (a–e) for all phase error values. Inset (f) shows results for $\beta$-peak shifted from 1.5 ppm (422.4 points) to 1.498 ppm (422.5 points). Inset (g) displays PAMPAS errors for $\alpha$-peak shifted from 4.1 ppm (289.28 points) to 4.1055 ppm (289 points). Inset (h) illustrates effects of $\beta$-peak shift to 1.508 ppm (422 points). Inset (i) displays PAMPAS errors for $\alpha$-peak at 4.096 ppm (289.5 points). No noise is present in insets (f–i). The data points, error bars, and continuous lines have the same meaning as in Figs. 2a–4a. Integration domain width is fixed at 29 points, with the exception of the lower curve in inset (f) (57 points).

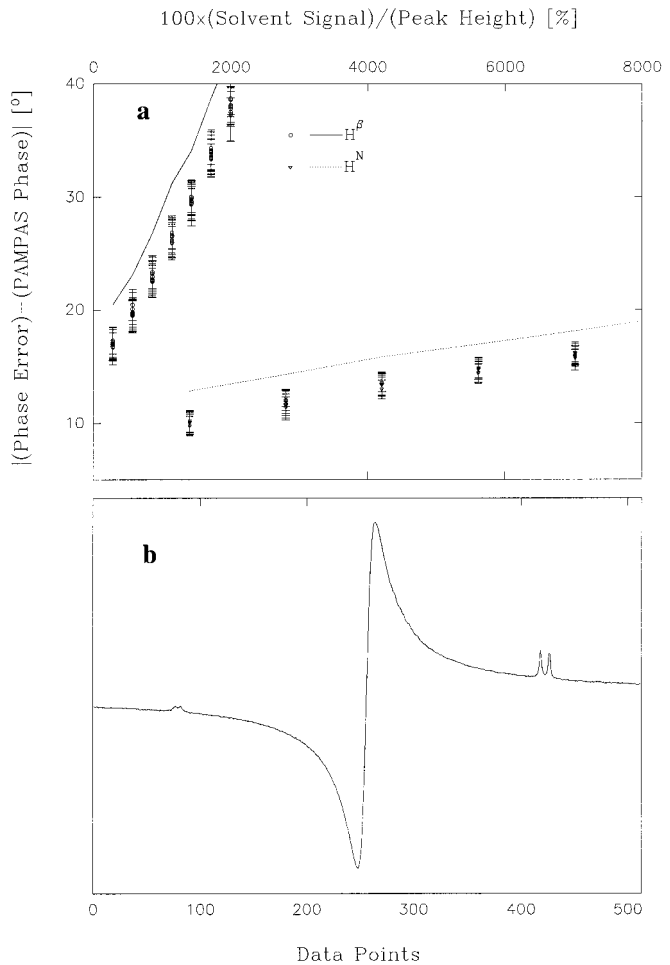


**FIG. 6.** (a) PAMPAS errors in spectra with increasing dispersive solvent signal at 4.75 ppm; (b) an example of a spectrum used to calculate data points in inset (a). Twenty noise sequences (−10.2 dB relative to the $\alpha$-peak) are used for each of eight equidistant phase errors (incremented by $\pi/4$). The data point symbols and lines are the same as in previous figures. The integration domain is 15 points wide.

the peak. This location usually is determined using a peak picking procedure. Relatively small errors in peak picking (caused, among other things, by the noise in the signal) can quickly degrade PAMPAS phases beyond resemblance to the true values. For example, to achieve phase correction accuracy of 10° or better, the difference between the actual and the measured peak positions must be less than one-fourth of the peak width when the integration domain is four times wider than the peak (Fig. 4a, open circles and triangles). The problem becomes even more severe when the integration domain is narrower (Fig. 4a, filled circles). The finite width of the integration domain is at the root of this problem. When the center of a finite integration domain does not coincide with the peak center, the integrals of the positive and the negative lobes of the dispersive component are not balanced and fail to cancel out. The nonvanishing contribution from the dispersive component to the measured peak area distorts the Fourier coefficients and results in wrong phase estimates. This observation suggests the solution: increase the width of the integration domain to reduce the influence of the dispersive component. The increased amount of noise is a small price for the accuracy gained.

Natural peak width is another potential source of problems that can be solved by adjusting the size of the integration domain. For best results, the PAMPAS integration domain should be at least twice as wide as the peak itself (preferably three times, see Figs. 3a and 11a). This requirement apparently limits the choice of peaks that can be treated with PAMPAS to those that are well separated from the rest of the peaks in a spectrum. This limitation is significantly relaxed by the fact that a group of overlapped peaks can be selected and successfully treated with PAMPAS as if it were a single peak, under the condition that the group is well separated from other peaks. The key factor here is the insensitivity of PAMPAS calcula-

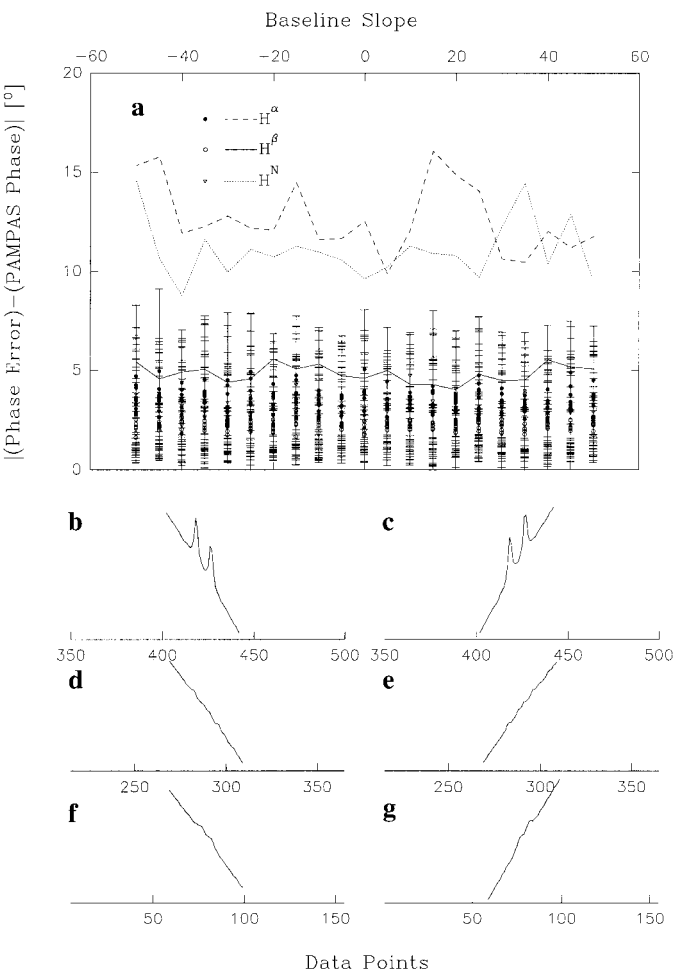


**FIG. 7.** (a) PAMPAS errors in spectra with increasing baseline tilts; (b–g) examples of peaks used to calculate data points in inset (a). The slope of the baseline is expressed in units of intensity per data point. Twenty noise sequences (−5.2 dB relative to the $\alpha$-peak) are generated per phase error value. The integration domain is 41 points wide. The symbols and lines are the same as in previous figures.

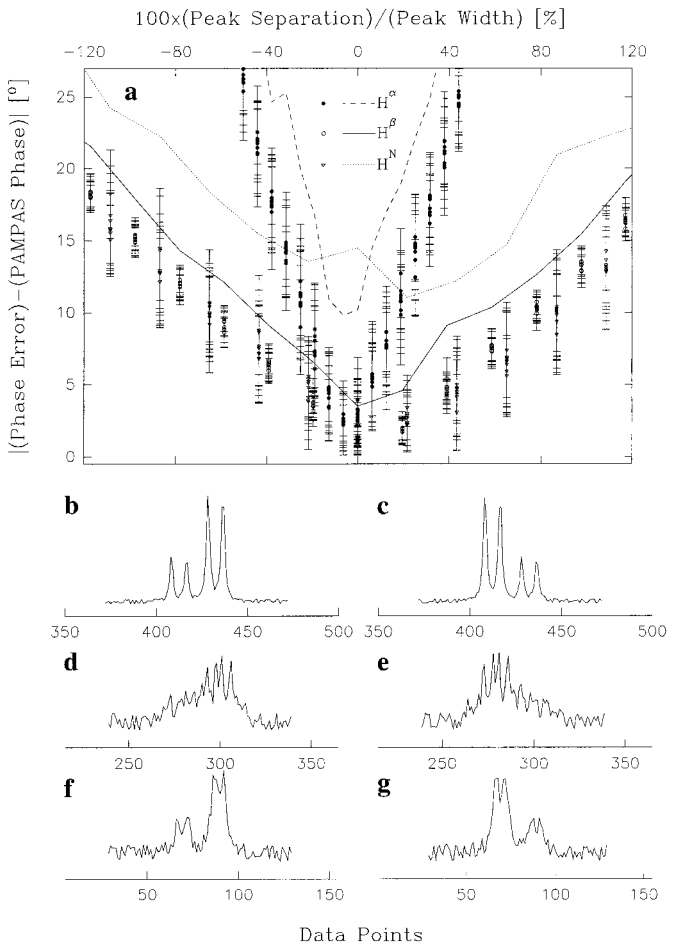


**FIG. 8.** (a) The effects of the peak overlap on PAMPAS results; (b–g) pairs of overlapping peaks used to calculate data points in inset (a). Data point symbols and continuous lines have the same meaning as in previous figures. Twenty noise sequences (−5.2 dB with respect to the $\alpha$-peak) are generated for each phase error ($n\pi/4$). Integration domains are 101 points wide.

tions to peak overlap (Fig. 8a), which is due to the fact that the basic equations (Eq. [2]) do not assume anything about the number of peaks within the integration domain or about their overlap: it holds for any number of overlapping peaks. The only requirement is that the phase remains uniform within the integration domain.

The PAMPAS integration domain can be centered anywhere within an asymmetric group of peaks as long as the integration domain is wide enough so that at least approximate cancellation is achieved for the dispersive components of the constituent peaks. This distinguishes PAMPAS from the methods based on lineshape analysis (*3, 8*), which break down when an asymmetric cluster of overlapping peaks is encountered. Similarly, when the integration domain is wide enough, PAMPAS results are barely affected by the inhomogeneity of the magnetic field and the resulting lack of symmetry of individual peaks.

Although the increase of the integration domain width solves a number of problems, it cannot be employed indefinitely. The maximum allowed width of the integration domain is limited by the requirement of uniform phase within the integration domain. If the first-order phase error cannot be neglected, the integration domain is too wide.

The unexpected asymmetry in Fig. 4a results from the fact that, in general, a peak position does not coincide with any of the discrete points where the spectrum is sampled. This leads to slight asymmetry of the integration domain, which starts and ends at the sampling points. Similarly, the contributions from the unbalanced dispersive tails can alternate between positive and negative values as the first-order phase correction increases (Figs. 5f–5i). The complications arising from incomplete can-

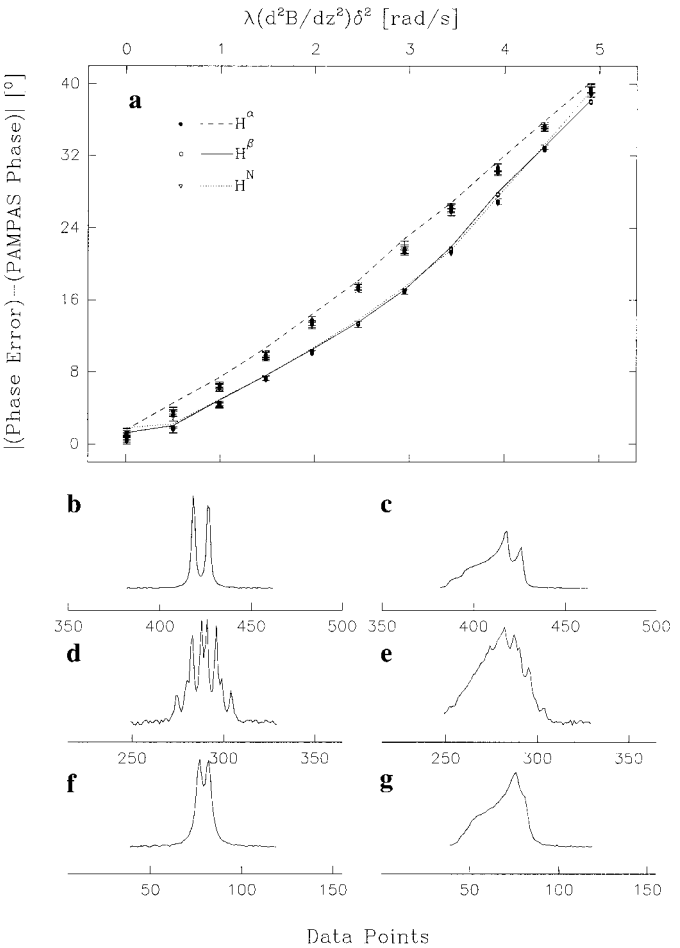


**FIG. 9.** (a) The dependence of PAMPAS errors on peak asymmetry; (b–g) examples of symmetric peaks in a homogeneous field (insets b, d, and f) and of asymmetric peaks in the presence of strong field gradient (insets c, e, and g; $\lambda(\partial^2 B/\partial z^2)\delta^2 = 5$ rad/s). Equations [A4, A5] (Appendix) are used to simulate effects of poor shimming on lineshapes. The product $\lambda(\partial^2 B/\partial z^2)\delta^2$ provides a measure for the field inhomogeneity (inset a, abscissa; see Appendix). Five noise sequences (−15.5 dB relative to the $\alpha$-peak in absence of the field gradient) are generated per phase error value. The integration domain width is equal to 81 points.

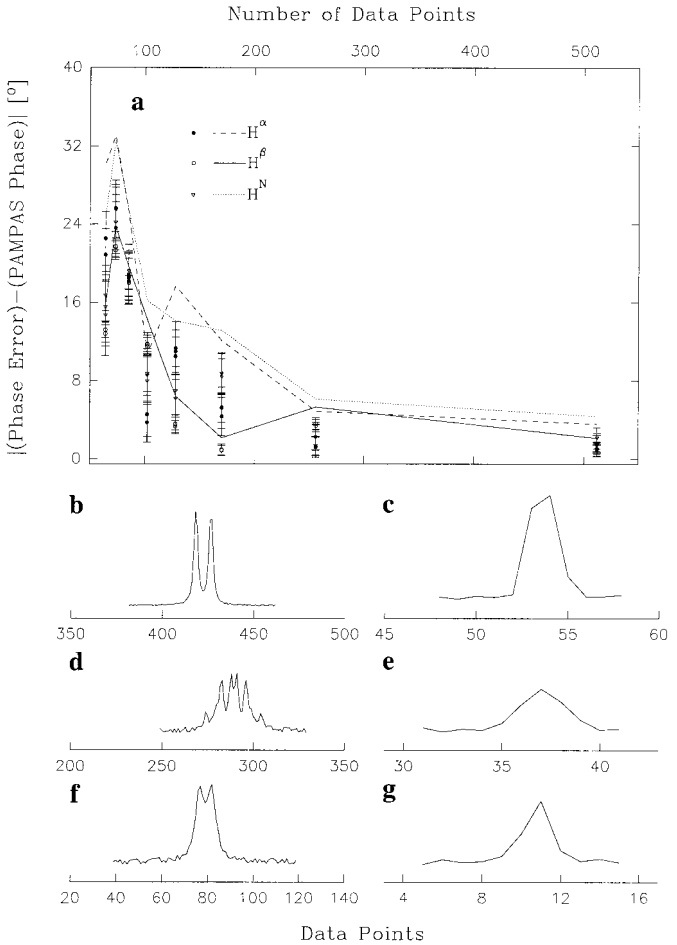


**FIG. 10.** (a) The effects of the digital resolution on PAMPAS results; (b–g) examples of peaks with the highest resolution (512 data points, insets b, d, and f ) and with the fewest data points (64, insets c, e, and g). The integration domain corresponding to the largest data size is 81 points wide and decreases proportionally with the data size. Twenty noise sequences (−10.2 dB with respect to the $\alpha$-peak) are generated for each phase angle value.

cellation of the dispersive tails are minimized when the sum of the true phase and the phase shift applied is close to zero.

Baseline imperfections caused by large first-order phase errors (Fig. 5a) or a wide range of tilts (Fig. 7a) fail to affect PAMPAS results. An intense unphased solvent peak, however, introduces significant errors in PAMPAS phase estimates (Fig. 6a). The errors arise due to nonlinearity of the solvent peak tail, which is not included in the model of the baseline. This further limits the widths of the integration domains in samples with strong solvent tails.

The spectral baseline in the immediate vicinity of the peak must be corrected before PAMPAS integration can be carried out. Two approaches were tested. Both subtract a straight line from the signal, approximating the baseline with a linear function of the frequency on the small segment of the spectrum occupied by the peak. The simpler approach uses a horizontal straight line positioned at the middle between the heights of the endpoints of the integration domain. The alternative is to use a tilted straight line that connects the endpoints. In both cases, the noise is suppressed by averaging several points at the ends of the domain. The two methods are equally successful when the baseline is linear and equally ineffectual when it is not. The simpler of the two is thus preferable. A variation that averages results obtained from multiple integration domain widths further reduces the effect of noise on the baseline correction and improves the phase estimates (not shown).

Insufficient number of data points and poor digital resolution decrease somewhat the accuracy of PAMPAS calculations (Fig. 10a) for the following reasons. First, the summation of data point values becomes a poor substitute for integration when data points are far away from one another. Also, the reduced number of data points across the integration domain

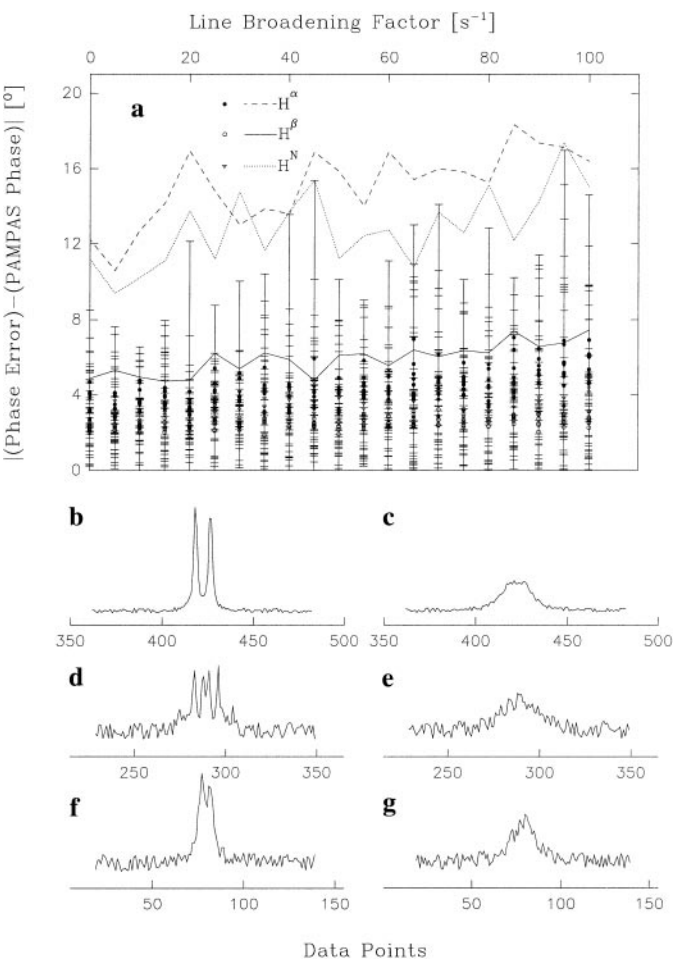


**FIG. 11.** (a) The effects of peak width; (b–g) comparison of peaks from the extremes of the line broadening range displayed in inset (a). Insets (b), (d), and (f ) show $\beta$, $\alpha$, and amide peaks, respectively, without line broadening. The same peaks are shown in insets (c), (e), and (g) after being subject to a line broadening factor of 100 $s^{-1}$. Integration domain width is equal to 41 points. Twenty noise sequences (−5.2 dB relative to the $\alpha$-peak) are generated for each of eight fixed phase errors. The same data point symbols and continuous lines are used as in previous figures.

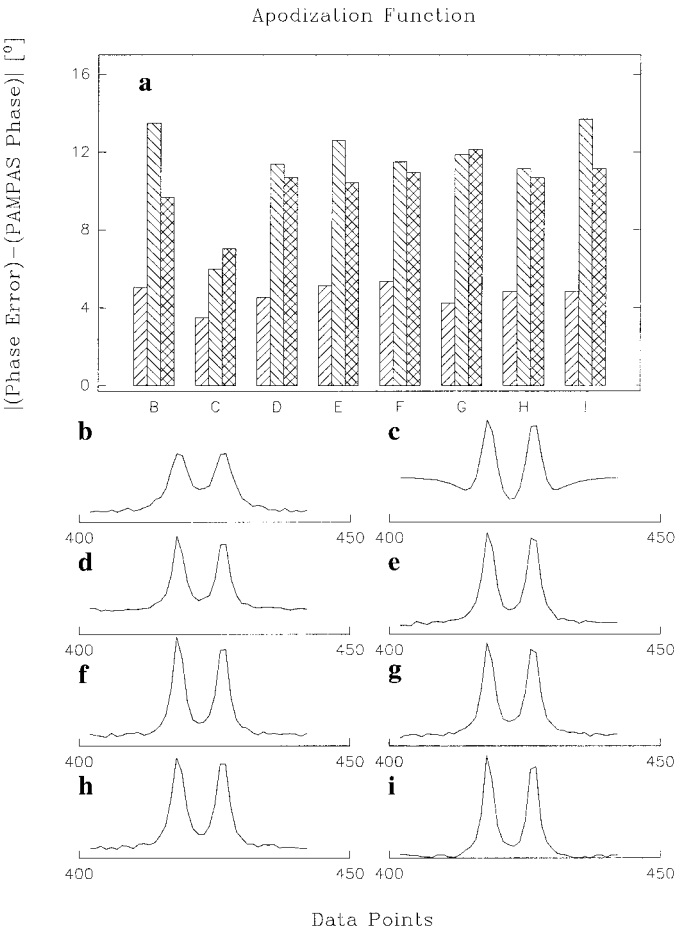


**FIG. 12.** (a) PAMPAS errors in spectra processed with different apodization functions: (b) exponential line broadening (line broadening = 20 $s^{-1}$), (c) Gaussian window (line broadening = $-20$ $s^{-1}$, Gaussian parameter = 0.2), (d) sine bell ($\pi/2$ phase shift, window covers all data points), (e) squared sine bell ($\pi/2$ phase shift, all data points), (f ) skewed sine bell ($\pi/2$ phase shift, all data points, unit skew), (g) skewed squared sine bell ($\pi/2$ phase shift, all data points, unit skew), (h) Kaiser window ($\alpha$ = 8 dB, all data points), and (i) trapezoidal function with the points of the trapezoid 10, data size–10, and data size. Insets (b–i) show the $\beta$-peak only. Bar groups labeled with letters B–I in inset (a) correspond to the apodization functions illustrated in insets (b)–(i), respectively. The left, middle, and right bars in each bar group of the histogram correspond to $\beta$, $\alpha$, and amide protons, respectively. The integration domain width is 41 points. Twenty noise sequences ($-5.2$ dB relative to the $\alpha$-peak) are generated per phase error value.

increases the impact of noise. Finally, the chances of picking an incorrect peak position increase when the peak is represented by fewer data points, mostly because the symmetry of the peak may not be evident (Figs. 10c, 10g). Since PAMPAS is relatively insensitive to peak asymmetry, the effect of digital resolution is smaller than in methods based on peak symmetry (*8*, *12*). Strong apodization functions, used to avoid ripples from FID truncation in data sets with fewer points, broaden the peaks but do not degrade PAMPAS results (see Fig. 11a).

The application of PAMPAS is by no means limited to the special cases 1–4 described above. PAMPAS imposes very few restrictions on the number of phase increments (Nyquist theorem) or their values. For example, in the special case 2, any value except $\pi$ can be used for $\Psi_2$. The value $\pi$ cannot be used for $\Psi_2$ because the matrix from Eq. [7] becomes singular when $N = 2$ and $|\Psi_2 - \Psi_1| = \pi$. Interestingly, Eqs. [14, 15] (case 4), although approximate, reduce to the exact Eq. [13] (case 3) when $N = 3$. Test calculations based on special cases 1–4 yield identical results (data not shown), but the special case 1 is preferred because it is the simplest and the quickest. Certain situations, however, require modifications in the algorithm. For example, when the denominators in Eqs. [10, 11] and [13, 14] are much smaller than the numerators, the initial phase of the peak should be shifted by an arbitrary amount different from $\pi$ prior to applying PAMPAS. The baseline correction (vide supra) is yet another example of how the results can be improved by picking the most suitable PAMPAS algorithm.

Note that Eqs. [8, 9] can be used to improve the accuracy of peak intensity measurements when peak phases are not perfect.

Unlike the grid-search procedures, where precision is achieved at the expense of speed (and vice versa), PAMPAS uses simple analytical relationships that demand minimal computational cost, yielding optimal peak phases whose precision depends primarily on errors in measured experimental input data. Another important strength of PAMPAS is its absence of dependence on the lineshape (Fig. 12a). The existing approaches that assume Lorentzian or Gaussian lineshapes (*3*, *6*, *7*) are clearly inferior to PAMPAS whenever NMR peaks deviate from those ideal shapes, a regular occurrence in real spectra (Fig. 1).

## 5. CONCLUSION

PAMPAS is accurate, fast, robust, and simple. Its superiority with respect to the methods based on lineshape analysis makes it the method of choice for automated phase correction. The effectiveness and robustness of PAMPAS in phase-correcting experimental ND NMR spectra is evidenced by Fig. 1. An implementation of PAMPAS has been incorporated into a new autophase routine within the FELIX software package for NMR processing and analysis (*14*), and it has proven successful in multidimensional spectra (manuscript in preparation).

## APPENDIX: ASYMMETRIC LINESHAPES IN INHOMOGENEOUS MAGNETIC FIELD

To study how PAMPAS phases depend on the quality of shimming, the following model of asymmetric lineshapes in an inhomogeneous magnetic field is used. A magnetic field gradient is introduced along the direction $z$ of the static field $B$. The spatial variation of the resonance frequency $\Omega_0$ is expanded into a Taylor series around the middle of the sample along the coordinate $z$:

$$\Omega_0 = \hbar\gamma(1-\sigma)\left[B_0 + \left(\frac{\partial B}{\partial z}\right)z + \frac{1}{2}\left(\frac{\partial^2 B}{\partial z^2}\right)z^2 + \cdots\right]$$
$$\approx \omega_0 + \lambda\left(\frac{\partial^2 B}{\partial z^2}\right)z^2. \qquad [A1]$$

The constants $\hbar$, $\gamma$, and $\sigma$ represent Planck's constant, the gyromagnetic ratio, and the magnetic shielding, respectively. The term $\omega_0$ is the value of $\Omega_0$ corresponding to the magnetic field $B_0$ at the middle of the sample:

$$\omega_0 = \hbar\gamma(1-\sigma)B_0 \quad \lambda = \frac{1}{2}\hbar\gamma(1-\sigma) = \omega_0/(2B_0). \qquad [A2]$$

The linear term is dropped from further consideration because it distorts the lineshape in a symmetric fashion and therefore is not a concern of this study. The absorptive NMR signal at the frequency $\omega$ is obtained by evaluating the following integral across the entire length $\delta$ of the sample along the direction $z$,

$$A(\omega) = \int_{-\delta/2}^{\delta/2} \frac{\Delta\, dz}{[\omega_0 + \lambda(\partial^2 B/\partial z^2)z^2 - \omega]^2 + \Delta^2}$$
$$= \sqrt{\frac{8}{\lambda(\partial^2 B/\partial z^2)}} \times \mathrm{Im}\left\{\frac{\mathrm{arctg}[\sqrt{\lambda(\partial^2 B/\partial z^2)\delta^2/(8(\omega_0 - \omega - i\Delta))}]}{\sqrt{\omega_0 - \omega - i\Delta}}\right\}, \qquad [A3]$$

where $\Delta$ represents the natural linewidth of the peak. After rearrangement, the final expression for the lineshape is obtained:

$$A(\omega) = \sqrt{\frac{2}{\lambda(\partial^2 B/\partial z^2)\sqrt{(\omega_0-\omega)^2+\Delta^2}}} \times \left\{\frac{c}{2}\ln\left[\frac{(1-ps)^2 + p^2c^2}{(1+ps)^2 + p^2c^2}\right] + s\left[\mathrm{arctg}\left(\frac{-pc}{1+ps}\right) - \mathrm{arctg}\left(\frac{pc}{1-ps}\right) + \frac{\pi}{2}(\mathrm{sgn}(1+ps) - \mathrm{sgn}(1-ps))\right]\right\}. \qquad [A4]$$

The following auxiliary variables are used:

$$p = \sqrt{\frac{\lambda(\partial^2 B/\partial z^2)\delta^2}{8\sqrt{(\omega_0-\omega)^2+\Delta^2}}} \quad s = \sin(\xi) \quad c = \cos(\xi)$$
$$\xi = \frac{1}{2}\,\mathrm{arctg}\left(\frac{\Delta}{\bar{\omega} - \bar{\omega}_0}\right) + \frac{\pi}{4}[\mathrm{sgn}(\omega_0 - \omega) - 1]. \qquad [A5]$$

The dispersive component is calculated by means of Hilbert transform. Equation [A4] reduces to the Lorentzian lineshape in the limiting case of homogeneous field.

## ACKNOWLEDGMENTS

The author thanks Drs. Sandor Szalma, Chen Peng, Steve W. Unger, Carol Gorst, and Teresa Lyons for valuable discussions. Drs. Tracy M. Handel (UC-Berkeley) and Peter J. Domaille (DuPont Merck) are acknowledged for collecting, assigning, and donating to MSI the 2D $^1$H–$^{15}$N HSQC spectrum of MCP-1.

## REFERENCES

1. R. R. Ernst, G. Bodenhausen, and A. Wokaun, "Principles of Nuclear Magnetic Resonance in One and Two Dimensions," Clarendon, Oxford (1987).
2. C. Cieslar, G. M. Clore, and A. M. Gronenborn, *J. Magn. Reson.* **79,** 154–157 (1988).
3. E. C. Craig and A. G. Marshall, *J. Magn. Reson.* **76,** 458–475 (1988).
4. D. E. Brown, T. W. Campbell, and R. N. Moore, *J. Magn. Reson.* **85,** 15–23 (1989).
5. E. A. Wachter, E. Y. Sidky, and T. C. Farrar, *J. Magn. Reson.* **82,** 352–359 (1989).
6. F. Montigny, K. Elbayed, J. Brondeau, and D. Canet, *Anal. Chem.* **62,** 864–867 (1990).
7. J. J. van Vaals and P. H. J. van Gerwen, *J. Magn. Reson.* **86,** 127–147 (1990).
8. A. Heuer, *J. Magn. Reson.* **91,** 241–253 (1991).
9. R. E. Hoffman, F. Delaglio, and G. C. Levy, *J. Magn. Reson.* **98,** 231–237 (1992).
10. P. Guntert, V. Dotsch, G. Wider, and K. Wuthrich, *J. Biomol. NMR* **2,** 619–629 (1992).
11. G. Balacco, *J. Magn. Reson. A* **110,** 19–25 (1994).
12. P. Koehl, C. Ling, and J. F. Lefevre, *J. Chim. Phys. Phys. Chim. Biol.* **92,** 1929–1938 (1995).
13. T. M. Handel and P. J. Domaille, *Biochemistry* **35,** 6569–6584 (1996).
14. "Felix User Guide, Version 98," MSI, San Diego (1998).